



**Quantitative Temporally and Spatially Resolved X-ray
 Fluorescence Microprobe Characterization of the Manganese
 Dissolution-Deposition Mechanism in Aqueous Zn/ α -MnO₂
 Batteries**

Journal:	<i>Energy & Environmental Science</i>
Manuscript ID	EE-ART-07-2020-002168.R1
Article Type:	Paper
Date Submitted by the Author:	23-Aug-2020
Complete List of Authors:	Wu, Daren; Stony Brook University, Materials Science and Chemical Engineering Housel, Lisa; Stony Brook University Kim, Sung Joo; Brookhaven National Laboratory, Interdisciplinary Science Sadique, Nahian; Stony Brook University, Chemistry Quilty, Calvin; Stony Brook University, Chemistry Wu, Lijun; Brookhaven National Laboratory Tappero, Ryan; Brookhaven National Laboratory, NSLS-II Nicholas, Sarah; Brookhaven National Laboratory Ehrlich, Steven; Brookhaven National Laboratory Zhu, Yimei; Brookhaven National Laboratory Marschilok, Amy; Stony Brook University, Chemistry Takeuchi, Esther; Stony Brook University, Materials Science and Engineering Bock, David; Brookhaven National Laboratory, Takeuchi, Kenneth; Stony Brook University, Chemistry

Quantitative Temporally and Spatially Resolved X-ray Fluorescence Microprobe Characterization of the Manganese Dissolution-Deposition Mechanism in Aqueous Zn/ α -MnO₂ Batteries

Daren Wu^{1†}, Lisa M. House^{1†}, Sung Joo Kim^{3,4}, Nahian Sadique², Calvin D. Quilty², Lijun Wu⁴, Ryan Tappero⁵, Sarah L. Nicholas⁵, Steven Ehrlich⁵, Yimei Zhu^{4,6}, Amy C. Marschillok^{1,2,3}, Esther S. Takeuchi^{1,2,3*}, David C. Bock^{3*}, Kenneth J. Takeuchi^{1,2*}

¹Department of Materials Science and Chemical Engineering, Stony Brook University, Stony Brook, New York 11794, United States

²Department of Chemistry, Stony Brook University, Stony Brook, New York 11794, United States

³Energy and Photon Sciences Directorate, Brookhaven National Laboratory, Upton, New York 11973, United States

⁴Condensed Matter Physics and Materials Science Department, Brookhaven National Laboratory, Upton, New York 11973, United States

⁵National Synchrotron Light Source II, Brookhaven National Laboratory, Upton, New York 11973, United States

⁶Department of Physics and Astronomy, Stony Brook University, Stony Brook, New York 11794, United States

* corresponding authors: (EST) esther.takeuchi@stonybrook.edu, (DCB) dbock@bnl.gov, (KJT) kenneth.takeuchi.1@stonybrook.edu

†authors contributed equally to the manuscript

Abstract

Rechargeable aqueous Zn/ α -MnO₂ batteries are a possible alternative to lithium ion batteries for scalable stationary energy storage applications due to their low cost, safety and environmentally benign components. A critical need for advancement of this battery system is a full understanding of the electrochemical reaction mechanisms, which remain unclear. In this report, *operando*, spatiotemporal resolved synchrotron x-ray fluorescence mapping measurements on a custom aqueous Zn/ α -MnO₂ cell provided direct evidence of a Mn dissolution-deposition Faradaic mechanism that governs the electrochemistry. Simultaneous visualization and quantification of the Mn distribution in the electrolyte revealed the formation of aqueous Mn species during discharge and depletion on charge. The findings are supported by *ex-situ* transmission electron microscopy (TEM), x-ray diffraction, Mn K-edge x-ray absorption near edge structure (XANES) and extended x-ray absorption fine structure (EXAFS) measurements. The elucidated mechanism is fundamentally different from the previously proposed Zn²⁺

insertion or conversion reactions. These findings provide a foundation for developing dissolution-deposition chemistries suitable for scalable stationary energy storage with aqueous electrolyte.

Broader context

Rechargeable aqueous zinc-manganese oxide (Zn/MnO₂) batteries are conceptually appealing as an alternative to commercial lithium ion batteries for large scale stationary energy storage, as their components (Zn, Mn) are earth-abundant, compatible with aqueous electrolytes, offer lower cost, improved safety and minimal environmental risk. To date, the literature suggests the charge storage mechanism of Zn/MnO₂ with mildly acidic ZnSO₄ electrolyte results from Zn²⁺ and/or H⁺ (co)insertion, which distorts the native structure of the MnO₂ host material. Herein is presented the first *operando* visualization and quantification of Mn dissolution and deposition during intermittent discharge, open circuit voltage, and under charge/discharge cycling via synchrotron-based x-ray fluorescence mapping. These data provide direct evidence that Mn²⁺ dissolution-deposition is the primary charge storage mechanism for the Zn/α-MnO₂ battery with aqueous ZnSO₄ electrolyte. This conclusive demonstration of a dominant Faradaic process governed by dissolution-deposition represents a paradigm shift regarding the fundamental mechanism of aqueous Zn/MnO₂ batteries, which can inform the field to implement improved cycle life batteries for scalable stationary energy storage.

Introduction

The consistent delivery of clean electrical energy is a global challenge where the current electric grid infrastructure distributes electrical energy from the generation source to the end user; however, once generated, the electrical energy must be used, or it is wasted.¹ In contrast, integration of electrical energy storage into the electric grid would enable control over when the electrical energy is used, improving grid reliability and resiliency as well as facilitating the incorporation of inherently intermittent renewable energy sources such as wind and solar.² Thus, stationary energy storage for the electric grid is a critical and timely application for battery technologies.

Aqueous batteries are desirable candidates for stationary energy storage due to low cost and scalability. In addition, many electrode materials compatible with aqueous electrolytes are earth abundant, and thus may be more cost effective than traditional lithium-ion battery materials.³ While batteries with aqueous electrolytes are less flammable than the non-aqueous organic electrolytes employed in lithium-ion battery technologies, they can still undergo problematic degradation processes.⁴ Thus, mechanistic understanding of promising aqueous battery chemistries is critical. Rechargeable aqueous Zn/MnO₂ batteries have received attention for large-scale energy storage application and multiple phases of MnO₂ have been considered.⁵⁻¹¹ Zn metal has a low redox potential (-0.76 V vs. SHE) and under mild acidic conditions exhibits an overpotential for hydrogen evolution, enabling a deposition and stripping charge storage mechanism when applied as a battery anode.¹² Zn is also non-toxic and has a high theoretical capacity (820 mA/g). Additionally, Zn metal batteries are advantageous relative to Li- and Na-ion aqueous systems, which often require intercalation host anodes and high concentration electrolytes to achieve a suitable electrochemical window.¹²⁻¹⁴ Thus, the Zn/MnO₂ system is a potentially high energy density, low cost, and environmentally-friendly chemistry suited for stationary energy storage.¹⁵

Zn/MnO₂ batteries have been reported to display several reaction mechanisms, including Zn²⁺ insertion, H⁺ insertion, and dissolution-deposition.¹⁶ In fact, dissolution-deposition has been conceptually viewed as a broadly applicable design approach to aqueous battery systems.¹⁷ A Faradaic Mn²⁺ dissolution-

deposition mechanism was first proposed in 1998 for a Zn/ δ -MnO₂ cell with ZnSO₄ electrolyte, where during discharge, a two-electron transfer process results in sequential MnOOH_(s) formation and Mn²⁺ dissolution, and upon charge, Mn²⁺ redeposits at the MnO₂ cathode.¹⁸ The electrochemistry of Zn/ δ -MnO₂ cell with ZnSO₄ electrolyte has been studied recently with investigation of δ -MnO₂ morphology¹⁹ and Mn²⁺ containing electrolyte.²⁰ *Operando* pH measurements for aqueous Zn/ β -MnO₂ batteries in a series of electrolytes based on 2 M ZnSO₄ electrolyte were used to construct pH-potential-diagrams of manganese and zinc describing active material dissolution at lower pH values and oxygen gas evolution at higher potentials >1.7 V.²¹

The α -MnO₂ cathode material is of interest due to the extended crystal structure consisting of edge and corner-sharing MnO₆ octahedral units arranged in a 2 x 2 tunneled framework providing an open framework which can facilitate ion (de)insertion.^{22, 23} Multiple studies have probed the charge/discharge mechanisms for Zn/ α -MnO₂ cells in ZnSO₄ electrolyte; however, the reported charge storage mechanisms differ.^{5, 6, 24-30} For example, HRTEM suggested a proton conversion mechanism for Zn/ α -MnO₂ cells with 2M ZnSO₄, where H⁺ ions react with MnO₂ to form MnOOH, while OH⁻ ions react with ZnSO₄ and H₂O in the electrolyte to form zinc hydroxide sulfate hydrate (ZnSO₄[Zn(OH)₂]₃ · xH₂O).⁵ Other findings have suggested that Zn²⁺ ions insert into α -MnO₂ to form spinel ZnMn₂O₄ or layered Zn_xMnO₂ phases.^{6, 24, 31} For example, powder x-ray diffraction and bright-field TEM with corresponding electron diffraction patterns suggested reversible formation to layered Zn-birnessite when Zn/ α -MnO₂ cells are cycled in ZnSO₄ electrolyte.²⁴ Additional *in-situ* XRD data suggested the layered discharge product was more closely related to Zn-buserite, with an interlayer spacing ~3 Å larger than Zn-birnessite.³² Further, an analogue of the mineral chalcophanite ((Zn, Mn)Mn₃O₇·3H₂O) has been identified as a product where the structure resembles that of layered Na-birnessite (Na₄Mn₁₄O₂₇·9H₂O).²⁴ The combined use of XRD, TEM and electrochemical analyses also suggested a H⁺/Zn²⁺ co-insertion mechanism.^{30, 33} In addition to structural instability of manganese oxide cathode,¹⁰ the formation of ZnSO₄[Zn(OH)₂]₃ · xH₂O and Mn²⁺ dissolution have been linked to capacity degradation for Zn/MnO₂ cells.^{5, 18} Improved capacity retention under galvanostatic cycling of Zn/ α -MnO₂ was demonstrated by utilizing low-ZnSO₄ electrolyte concentrations below 0.2 M, attributed to suppression of cathode dissolution and mitigation of the formation of impurity phases such as ZnMn₂O₄ and ZnMn₃O₇ · xH₂O.³⁴ Recently, Mn²⁺ dissolution-deposition has been proposed to be a primary contributor to electrochemical capacity of Zn/MnO₂ (α -MnO₂ and δ -MnO₂) cells with mildly acidic aqueous electrolyte.³⁵

While the studies above have advanced understanding of the electrochemical mechanism for Zn/ α -MnO₂ using *ex-situ* XRD and SEM/TEM, *operando* evidence quantifying the impact of Mn dissolution/deposition on electrochemistry has been lacking. *Operando* and *in-situ* characterization using synchrotron radiation represents a forefront in battery research, enabling real-time observation of charge storage mechanisms in multiple battery systems under dynamic conditions.³⁶⁻³⁸ Moreover, the use of x-ray fluorescence spectroscopy can elucidate changes of the elemental distribution within an electrode after electrochemical cycling,^{39, 40} however, this technique only recently been applied *operando* as data collection has been previously limited by slow stage speeds and long mapping times.

For the first time, we provide direct evidence that demonstrates Mn dissolution and deposition is the dominant charge storage reaction in aqueous Zn/ α -MnO₂ cells by quantifying the relative contributions of dissolution and deposition to the electrochemistry. A synchrotron-based x-ray fluorescence mapping approach is applied to obtain novel spatio-temporally resolved distribution maps of Mn in a custom aqueous Zn/ α -MnO₂ electrochemical cell, where the mapping is conducted *operando* during intermittent

discharge, open circuit voltage, and under charge/discharge cycling. Complementary *ex-situ* x-ray diffraction (XRD), transmission electron microscopy (TEM), Mn K-edge x-ray absorption near edge structure (XANES) and extended x-ray absorption fine structure (EXAFS) measurements describe the evolution of bulk and local crystallographic structure. These findings represent a paradigm shift in understanding aqueous Zn/MnO₂ batteries and provide a pathway toward developing dissolution-deposition chemistries that enable the realization of scalable stationary energy storage.

Experimental

Synthesis of α -MnO₂ nanotubes: Hydrothermal synthesis of α -MnO₂ was adapted from a previously reported method.⁴¹ A solution of KMnO₄ dissolved in aqueous hydrochloric acid was heated at 140°C for 36h in an autoclave. Reaction products were washed with deionized water, dried, and calcined at 300°C in air for 6 hours prior to use.

Material characterization: X-ray diffraction (XRD) was performed using a Rigaku SmartLab X-ray diffractometer with Cu K α radiation and Bragg-Brentano focusing geometry. Water content was estimated from thermogravimetric analysis (TGA) using a TA instrument SDT Q600 under nitrogen. The ratio of K/Mn in the synthesized materials was determined from inductively coupled plasma spectrometry-optical emission spectroscopy (ICP-OES) using a Thermofisher iCap 6300 series instrument. TEM (transmission electron microscopy) and STEM (scanning TEM) images, SAED (selected area electron diffraction) patterns, and EELS (electron energy loss spectroscopy) spectra of pristine, discharged, and charged α -MnO₂ were acquired using a JEOL ARM 200F microscope, operated at 200 kV, equipped with double spherical aberration correctors (CEOS GmbH) and GIF Quantum ER Energy Filter (Gatan). Some STEM images were filtered to reduce the image background noise.

Electrode preparation and electrochemical measurements. As-synthesized α -MnO₂ nanotubes and multi-wall carbon nanotubes (Cheap Tubes, USA) were dispersed in pure ethanol via sonication in a mass/mass ratio of 1:1, then filtered to form a composite electrode. Coin type or *operando* cells were assembled using the electrodes, glass fiber separators and Zn foil with aqueous 2 M ZnSO₄ as the electrolyte. Galvanostatic cycling test was conducted using a Maccor testing system at 30°C. (Dis)charged samples for TEM, *ex-situ* XRD, *ex-situ* XAS, and *operando* XAS were collected using a current density of 150 mA/g.

Post-electrochemical testing characterization. Both charged and discharged α -MnO₂ electrodes were recovered, rinsed with deionized water and vacuum-dried. XRD was performed using a Rigaku Smartlab Diffractometer with copper K α radiation. Rietveld refinements were conducted using GSASII.⁴² A background peak was added to model the multiwalled carbon nanotube (MWCNT) diffraction signal. Mn K-edge x-ray absorption near edge structure (XANES) and extended x-ray absorption fine structure (EXAFS) measurements were collected at 7-BM of the National Synchrotron Light Source II (NSLS-II) at Brookhaven National Laboratory. All spectra were aligned, merged, deglitched and normalized using Athena.⁴³ Linear Combination Fitting (LCF) of the XANES data was executed with MnO₂ and Mn₂O₃ standards and fitting range from 6537 eV to 6587 eV. The built-in AUTOBK algorithm was utilized to minimize background contributions below $R_{\text{bkg}} = 1.0 \text{ \AA}$. All EXAFS spectra were fit using models derived from the α -MnO₂ $I4/m$ K_{1,33}Mn₈O₁₆ crystal structure⁴⁴ and the zinc-inserted chalcophanite $\bar{p}1$ ZnMn₃O₇·3H₂O crystal structure⁴⁵ with theoretical models created *via* FEFF6.^{43, 46} Each spectrum was fit using a k -range of 2.0–12.0 \AA^{-1} and a Hanning window ($dk = 2$) in k , k^2 and k^3 k -weightings simultaneously. The fit was conducted over an R -range of 1.0–3.6 \AA to fully encompass the neighboring Mn-O and Mn–

Mn coordination shells. For models based on cryptomelane (potassium α - MnO_2), distinct Mn–Mn coordination paths (edge-sharing octahedra along the c -axis, edge-sharing octahedra along ab plane, one corner sharing octahedra) were fit using the model, and coordination numbers of edge sharing versus corner sharing paths were allowed to vary independently. To account for intrinsic losses in the electron propagation and scattering processes, an amplitude reduction factor (S_0^2) of 0.76 was determined from modeling a MnO standard and was applied to all experimental fits. All presented fits resulted in combined R -factors less than 2.0% over the fitted range. Full fitting results are presented in the ESI.

Operando measurements: A custom designed *operando* cell with x-ray transparent housing was utilized to visualize Mn species in the cell during electrochemical measurements including the active Zn-separator-cathode cell stack with 2 M ZnSO_4 electrolyte. *Operando* μ -XRF mapping images were acquired using the XFM Beamline (4-BM) at National Synchrotron Light Source II (NSLS-II). Briefly, this beamline uses Kirkpatrick-Baez (KB) mirrors to deliver focused X-rays (2 - 10 μm spot) with tunable energy using a Si(111) double crystal monochromator (Si(220) and Si(311) also available). The sample was oriented 45° to the incident beam and the XRF detector (Hitachi 7-element Vortex SDD) was positioned 90° to the incident beam. Images were collected by continuously rastering the sample in the microbeam using a Newport stage with a 10 μm step size and 50 ms dwell time per pixel for course navigation maps, and a 2 μm step size and 100 ms dwell time per pixel for fine resolution maps. For μ -XRF imaging, the monochromator was calibrated using a manganese metal foil and was set to a fixed energy of 6.8 keV to excite the Mn K edge. Data acquisition was performed using Python-based beamline software developed for NSLS II 4-ID. Data visualization and analysis was performed using Larch analysis package⁴⁷ and Matlab.

Result and discussion

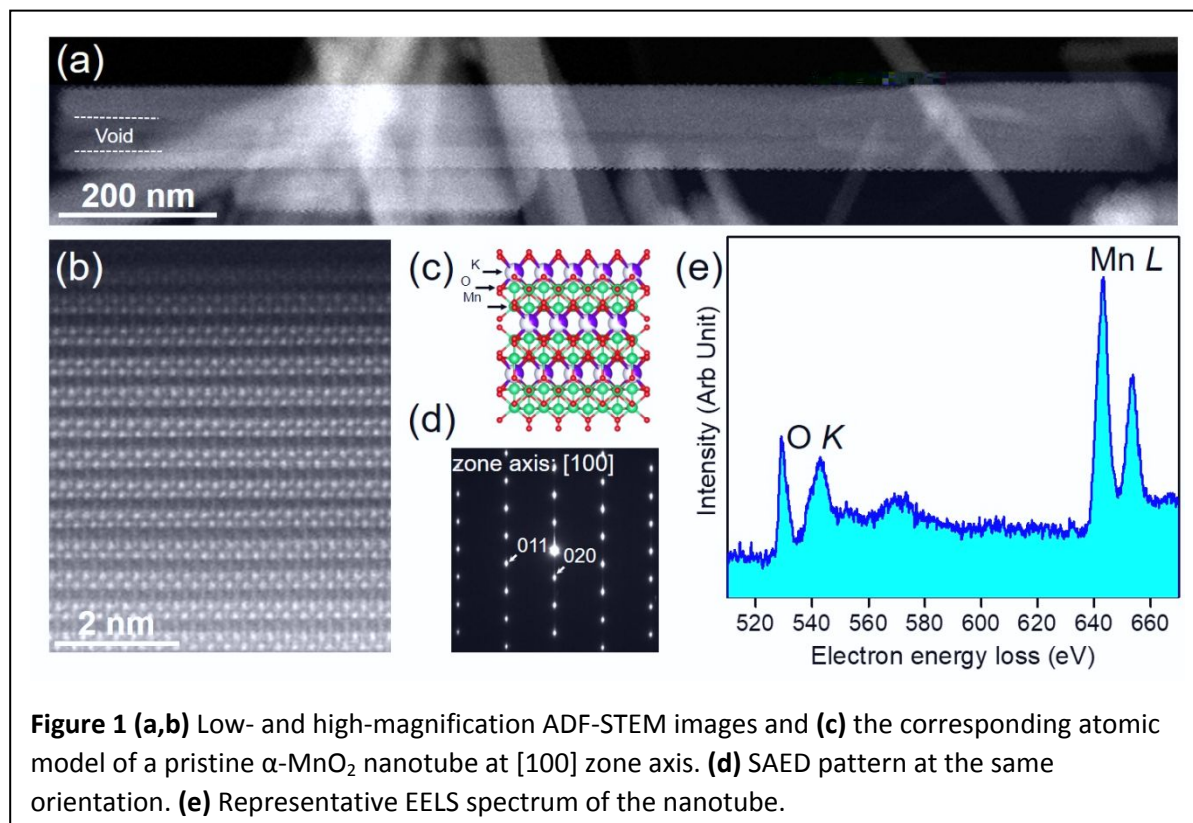
Phase composition of pristine and cycled cathodes

XRD patterns collected for the as-synthesized pristine material match the reference (PDF# 042-1348) as shown in **Figure S1**. Potassium α - MnO_2 has a 2 x 2 tunnel structure extending in the (0 0 1) direction with Mn octahedra forming the tunnel wall and K^+ occupying the tunnel center⁴⁸. Due to the presence of K^+ ions, Mn positioned at the tunnel walls are of a mixed Mn(III)/Mn(IV) oxidation state. The potassium/manganese ratio was measured to be K:Mn = 0.97:8 via ICP-OES. The water content was estimated by TGA (**Figure S2**) with a previously reported method.^{49, 50} Thus, the chemical formula can be written as $\text{K}_{0.97}\text{Mn}_8\text{O}_{16} \cdot 0.56\text{H}_2\text{O}$.

Figure 1 demonstrates the ADF (annular dark field)-STEM image of the typical nanorod with the large void located in the middle as a result of the synthesis method. Both high-resolution STEM imaging (**Figure 1(b)**) and representative electron diffraction (**Figure 1(d)**) taken at the [100] zone axis reveal high crystallinity of the nanorod. An EELS spectrum of a nanorod reveals the characteristic Mn L edge and O K edge of $\text{K}\alpha$ - MnO_2 (**Figure 1(e)**). The calculated Mn oxidation state from the Mn L_3/L_2 ratio is 3.83.

The synthesized α - MnO_2 was used as a cathode material for Zn/ α - MnO_2 aqueous batteries. Galvanostatic cycling was conducted at a current density of 150 mA/g. From **Figure 2(a)** and **(b)**, it can be seen that except for the initial discharge, subsequent cycling curves have consistent features. An activation process is observed through the first 5 cycles where the discharge and charge capacities converge. (**Figure 2(b)**) The initial discharge has one potential plateau at ~ 1.2 V, subsequent discharges consist of three plateaus at around 1.45 V, 1.3 V and 1.2 V, respectively. Among them, the third plateau at 1.2 V can be regarded as part of the initial activation process since it overlaps very well with initial discharge plateau. The third

plateau is no longer observed in the 5th cycle, indicating the end of activation process. Charge curves all have the same feature with a potential plateau at ~ 1.5 V.



XRD patterns were collected after cycle 1 and cycle 5 discharge/charge and compared to an undischarged electrode, **Figure 2(c)**. Rietveld refinement was conducted to determine phase composition of the pristine, discharge, and charge products. The α - MnO_2 -CNT electrode was refined with a cryptomelane reference phase (PDF # 00-020-0908) as shown in **Figure S3** and **Table S1**. α - MnO_2 contains a 2×2 tunnel structure that extends in the $(0\ 0\ 1)$ direction with Mn octahedra forming the tunnel and K^+ occupying the tunnel center.⁵¹ Due to the tunnel-like nature of the material, thermal parameters were modified for potassium ion occupancy in the refinement. All of the peaks can be attributed to the cryptomelane structure (space group = $I4/m$, $a = 9.8$ Å, $c = 2.8$ Å) with no detectable impurities and a goodness of fit of $\%R_{wp} = 3.205$. The unit cell and the atomic positions are in good agreement with the literature.⁵² The pristine α - MnO_2 -CNT electrode pattern demonstrates a peak at $\sim 25^\circ$ due to the presence of the CNT.⁵³ The CNT peak was treated as part of the background for the pristine and all subsequent fits.

On discharge, the XRD pattern refinements indicate the formation of triclinic zinc hydroxide sulfate hydrate $\text{Zn}_4\text{SO}_4(\text{OH})_6 \cdot 5\text{H}_2\text{O}$, ZHS (osakaite). The Rietveld refinement (**Figure S4**, **Table S2**) performed on the first discharge XRD pattern indicates a composition of 64% cryptomelane (PDF # 00-020-0908) and 36% ZHS (PDF # 00-067-0055). Upon charge, only the cryptomelane phase is present (**Figure S5**, **Table S3**), similar to the pristine electrode (**Figure S3**, **Table S1**).

The composition of the electrode after the 5th discharge is 42% cryptomelane and 58% ZHS, indicating that the ZHS content increases in the discharge product as cycling progresses (**Figure S6**, **Table S4**). Rietveld refinement of the XRD pattern after the 5th cycle charge (**Figure S7**, **Table S5**) indicates 78% of the

electrode is broken tunnel cryptomelane and the remaining 22% is a Zn-inserted layered chalcophanite ($\text{ZnMn}_3\text{O}_7 \cdot 3\text{H}_2\text{O}$) phase. Crystal structures for broken tunnel cryptomelane have been generated previously for lithiated $\alpha\text{-MnO}_2$ via density functional theory.⁵⁴ The layered structure of $\text{ZnMn}_3\text{O}_7 \cdot 3\text{H}_2\text{O}$ resembles Na or K-birnessite ($\delta\text{-MnO}_2$). However, $\text{ZnMn}_3\text{O}_7 \cdot 3\text{H}_2\text{O}$ is triclinic as opposed to monoclinic like

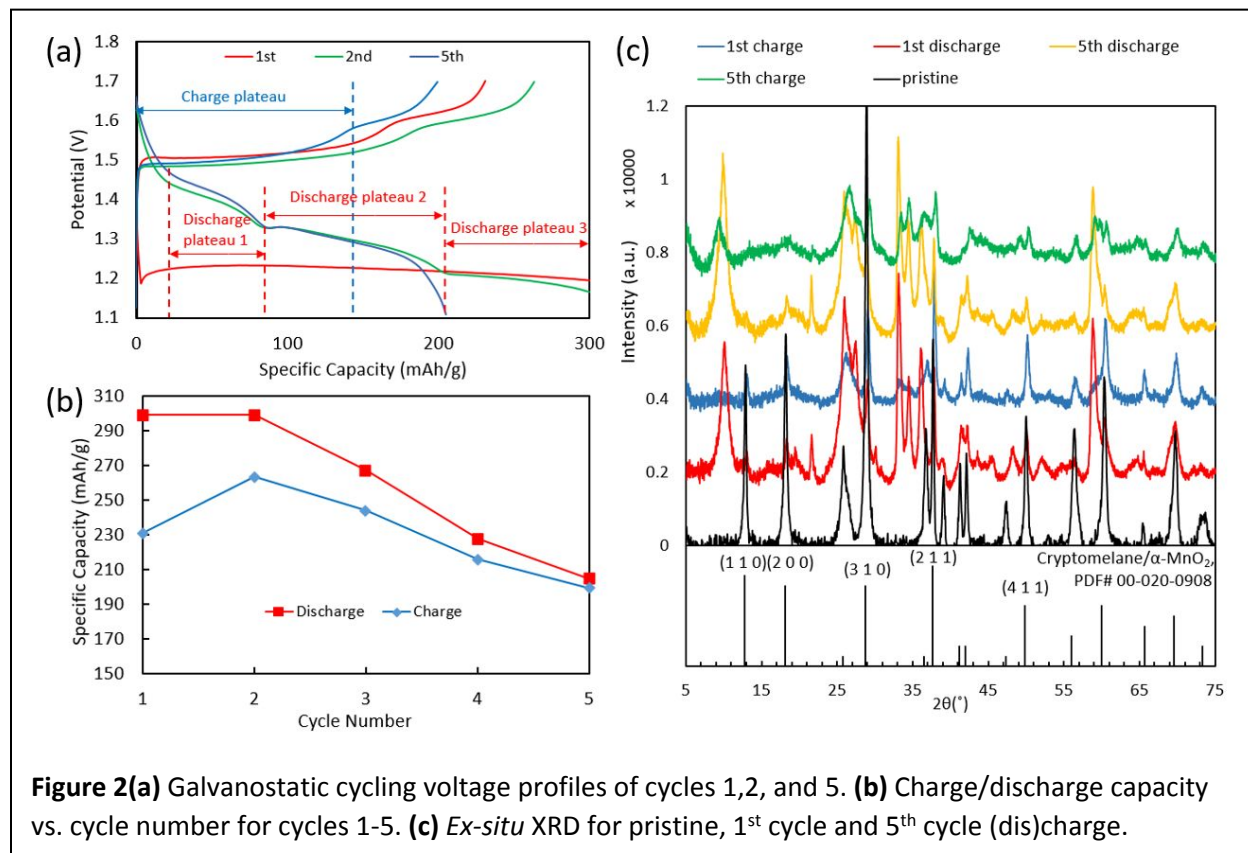


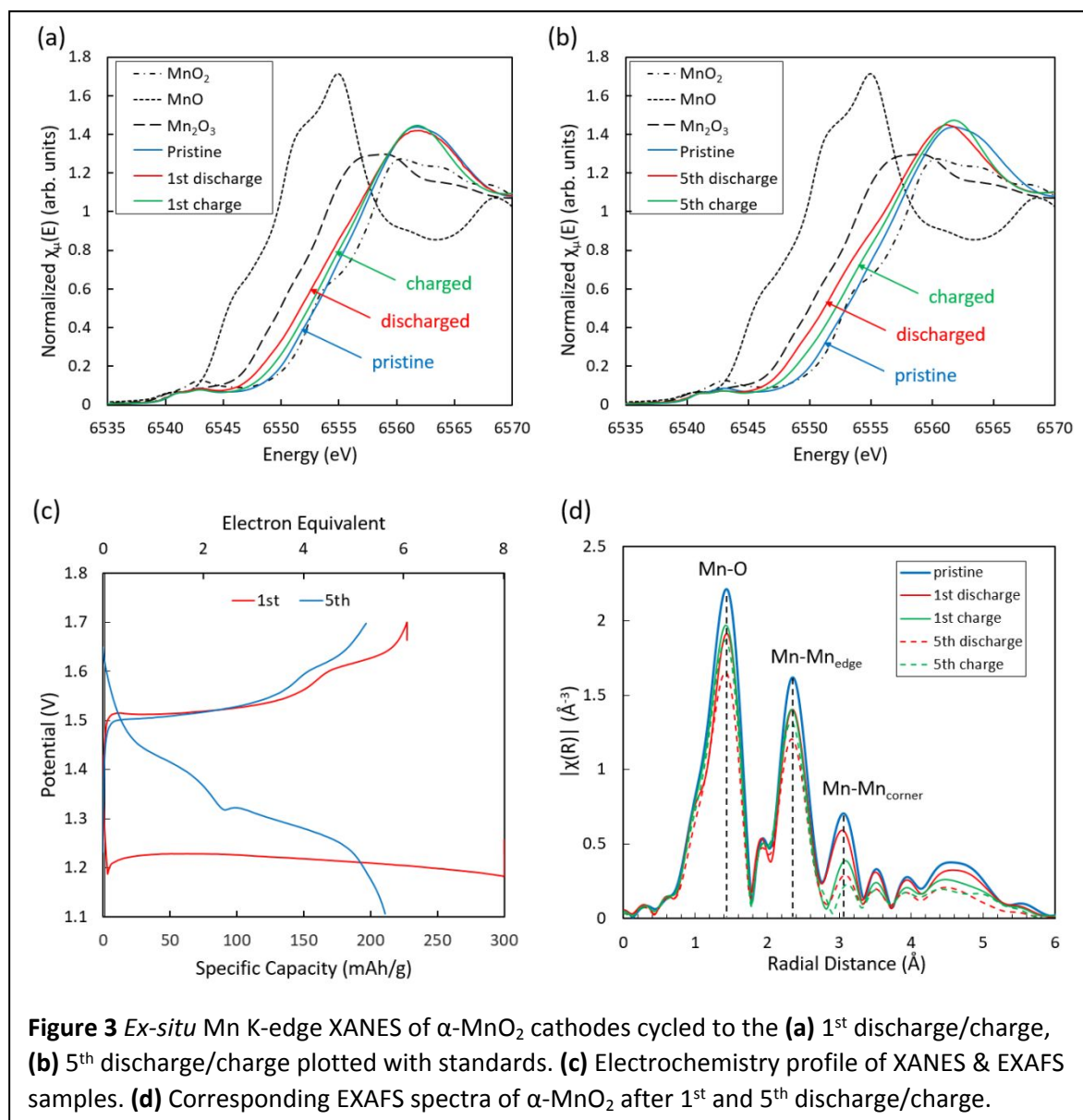
Figure 2(a) Galvanostatic cycling voltage profiles of cycles 1,2, and 5. **(b)** Charge/discharge capacity vs. cycle number for cycles 1-5. **(c)** *Ex-situ* XRD for pristine, 1st cycle and 5th cycle (dis)charge.

$\delta\text{-MnO}_2$, with Zn^{2+} ions located above and below the Mn vacancy sites and coordinated either tetragonally or octahedrally depending on Zn^{2+} content.^{45, 55} The $\text{ZnMn}_3\text{O}_7 \cdot 3\text{H}_2\text{O}$ phase has been previously reported to be a Zn^{2+} insertion product for $\alpha\text{-MnO}_2$ electrodes.²⁴

Chemical state and local structure of pristine and cycled cathodes

Ex-situ Mn K-edge x-ray absorption near edge structure (XANES) and extended x-ray absorption fine structure (EXAFS) measurements were collected for cathodes cycled to the 1st discharge, 1st charge, 5th discharge, and 5th charge. In **Figure 3(a)** and **(b)**, the Mn K-absorption edges of discharged samples from both the 1st cycle and 5th cycles shift slightly to lower energy with the energy levels between the Mn_2O_3 and MnO_2 reference standards, suggesting an oxidation state between Mn(III) and Mn(IV). Upon cycle 1 and cycle 5 charge, the absorption edges of both samples increase slightly. Linear combination fit (LCF) was used to estimate the Mn oxidation state. The Mn oxidation state of the pristine electrode is 3.88 and comparable to the Mn oxidation state determined by EELS for the as-synthesized powder (**Figure 1(e)**). Upon the first discharge, the LCF determined Mn oxidation state decreases slightly to 3.60. After the 1st charge, the oxidation state increases to 3.74. Similarly, the Mn oxidation state upon the 5th discharge is 3.47, which increases to 3.67 upon the 5th charge. This observation is significant because Mn oxidation state change in the cathode between charged and discharged samples transfers less than 0.2 electron

equivalent per metal center and does not fully account for the capacity observed in electrochemistry. For example, the first discharge delivers a specific capacity of 300 mAh/g equivalent to an ~ 8 electron transfer or ~ 1 electron equivalent per Mn center (**Figure 3(c)**). In contrast, delivered specific capacities predicted from LCF determined oxidation state range from 40-80 mAh/g, which is significantly less than the observed delivered specific capacities (**Table S6**).



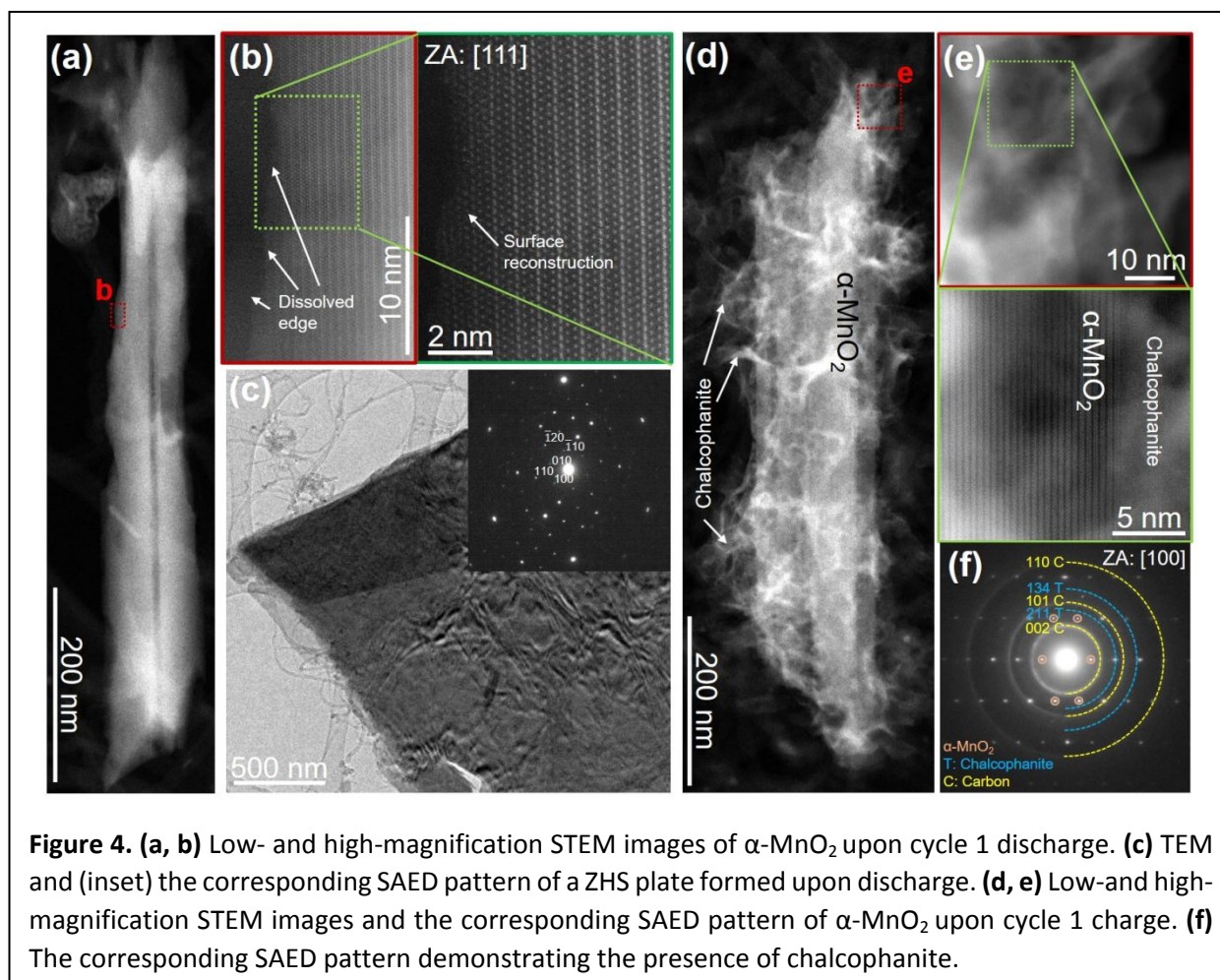
The evolution of the local structure of the α -MnO₂ cathode material was probed using extended x-ray absorption fine structure (EXAFS) spectroscopy. The Fourier transformed EXAFS spectra of the pristine, 1st cycle, and 5th cycle discharged and charged electrodes are shown **Figure 3(d)**. The pristine sample exhibits peaks at 1.5 Å, 2.3 Å, and 3.1 Å, which correspond to Mn-O, Mn-Mn_{edge}, and Mn-Mn_{corner} features, respectively, of tunnel structured α -MnO₂. During (dis)charge, the peaks corresponding to Mn-O and Mn-Mn_{edge} paths exhibit small variation in peak shift and intensity variation, while a consistent decrease in intensity is observed for the Mn-Mn_{corner} peak.

The EXAFS data was modeled to elucidate changes in the structure. Modeled coordination numbers and interatomic distances for all Mn-Mn paths are presented in **Figure S8**, and full fitting results are presented in **Table S7**. For the pristine electrode, the data fit well to a model derived from the α -MnO₂ *I4/m* K_{1.33}Mn₈O₁₆ crystal structure, with three distinct Mn-Mn paths (edge-sharing octahedra along the *c*-axis, edge-sharing octahedra along *ab* plane, corner sharing octahedra).⁴⁴ All fitted coordination values are within error of the theoretical values (CN = 2 for each edge sharing octahedra, CN=3 for corner sharing Mn octahedra). During the first discharge and charge, small changes in the coordination number of Mn-Mn_{edge} paths are observed, with values decreasing on discharge and increasing on charge. This result suggests a low but significant increase in structural distortion during discharge, consistent with Jahn–Teller distortion of the reduced manganese species.^{56–59} Markedly, as the samples are discharged and charged, no significant shift in first or second shell interatomic distance is observed in the 1st (dis)charge or 5th discharge, suggesting minimal insertion of Zn²⁺ ions into the host structure.

The most notable trend observed from the EXAFS modeling results is the continuous decrease in the fitted coordination number of the Mn-Mn corner sharing octahedra. The sample in the cycle 1 charge state shows that the Mn-Mn_{corner} coordination number drops to ca. 1.5, approximately half of the theoretical value for α -MnO₂ and continues to fall to ca. 1.3 by the 5th discharge. These findings indicate that significant breakage of the tunnel structure occurs during cycling consistent with the XRD results described above. By the 5th charge, the α -MnO₂ based model does not effectively describe the experimental spectra due to the significant loss of amplitude in the Mn-Mn_{corner} path. Fitting the 5th charge spectra to a model derived from layered chalcophanite, ZnMn₃O₇·3H₂O, with a Mn-Mn edge sharing path at ca. 2.87 and no corner sharing paths, results in a good fit with combined R factor = 0.5%. Thus, the EXAFS modeling results suggest that (1) the initial α -MnO₂ structure is altered during discharge due to breakage of the tunnel structure at corner sharing MnO₆ octahedra, and (2) a layered phase free of corner sharing octahedra is formed during charge. By the 5th charge, significant phase transformation has occurred such that Mn-Mn corner sharing octahedra are minimally or no longer present.

The results above are confirmed by TEM analysis. **Figure 4** demonstrates the ADF image of α -MnO₂ after cycle 1 discharge and charge. Upon discharge (**Figure 4(a)** and **4(b)**), reduced inter-planar spacing and some structural degradation attributed to dissolution are observed, with retention of the α -MnO₂ parent gross morphology and bulk structure. A SAED pattern (**Figure 4c** inset) from the plate in **Figure 4c** resembles the (001) plane diffraction pattern of Zn₄SO₄(OH)₆·5H₂O (ZHS, osakaite). The pattern indexing is done based on the pattern of ZHS. Upon charge, porous hairy sheets surrounding the nanotube surface are present (**Figure 4d** and **e**). From the electron diffraction in **Figure 4f**, these sheets are likely chalcophanite ZnMn₃O₇·3H₂O, which are reported to form upon electrochemical charge of α -MnO₂.²⁹

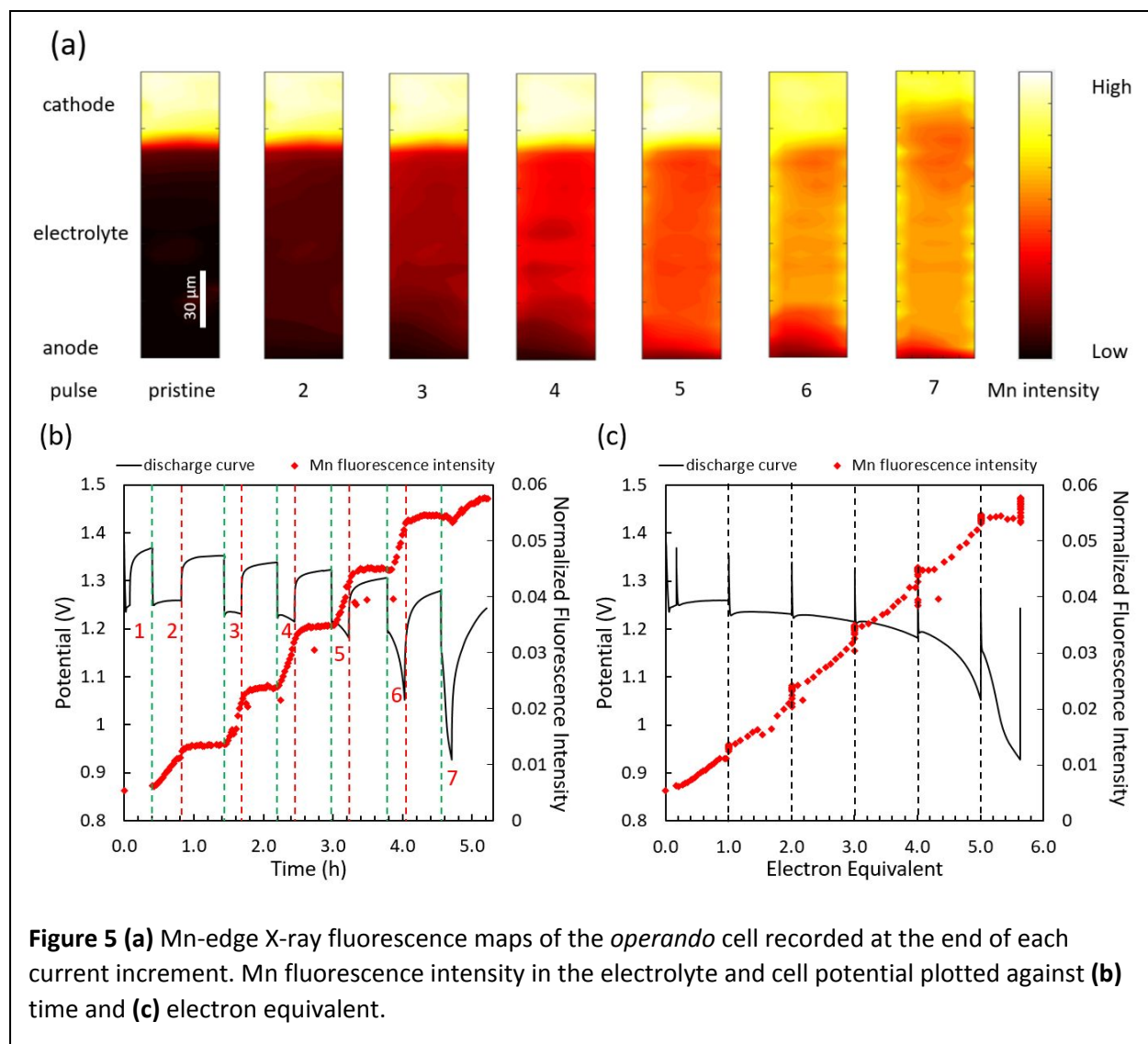
XRD, EXAFS, and TEM data suggest the active material in the recovered *ex-situ* discharged and charged electrodes remains as α -MnO₂ or related phases for the initial cycles, and as the cycling extends, a layered structure is observed. Further, the *ex-situ* XANES results show that the Mn in the electrodes is not sufficiently reduced or oxidized upon cycling to fully account for the capacity delivered. Thus, other possible reaction routes such as the reduction of Mn(III/IV) to Mn(II) accompanied by dissolution in the electrolyte were considered.



Direct observation of electrochemically induced Mn dissolution

Using the X-ray Fluorescence Microprobe (XFM) at NSLS-II, spatio-temporal Mn distribution maps were collected *operando* in an x-ray transparent Zn/ α - MnO_2 cell (**Figure S9**), resolving Mn distribution in the cathode and the electrolyte both visually and quantitatively. The *operando* cell configuration demonstrates comparable galvanostatic cycling profiles to the coin cell configuration used for *ex-situ* -TEM, XAS, and XRD characterization (**Figure S10**). In **Figure 5**, a Zn/ α - MnO_2 *operando* cell was discharged in 15-minute increments at 150 mA/g, followed by a 30-minute open circuit potential rest. During the intermittent discharge, Mn fluorescence maps, which encompass the α - MnO_2 cathode, 2 M ZnSO_4 electrolyte and Zn anode were collected every two minutes. After each current pulse (**Figure 5(a)**), the Mn fluorescence maps showed an increase in the Mn fluorescence intensity observed in the electrolyte, indicating an increase in Mn dissolution from the cathode after each discharge increment. The intermittent discharge voltage profile is shown as a function of time (**Figure 5(b)**) and compared to the Mn fluorescence intensity measured in the electrolyte. When current is applied, the Mn intensity increases and is directly related to the discharge. In contrast, during the 30-minute rest period, the Mn intensity changes minimally. In **Figure 5(c)**, the Mn fluorescence intensity is plotted versus the delivered electron equivalents during reduction per Mn_8O_{16} unit, demonstrating Mn intensity in the electrolyte

increases with state of discharge. This experiment demonstrates conclusively that Mn dissolution from

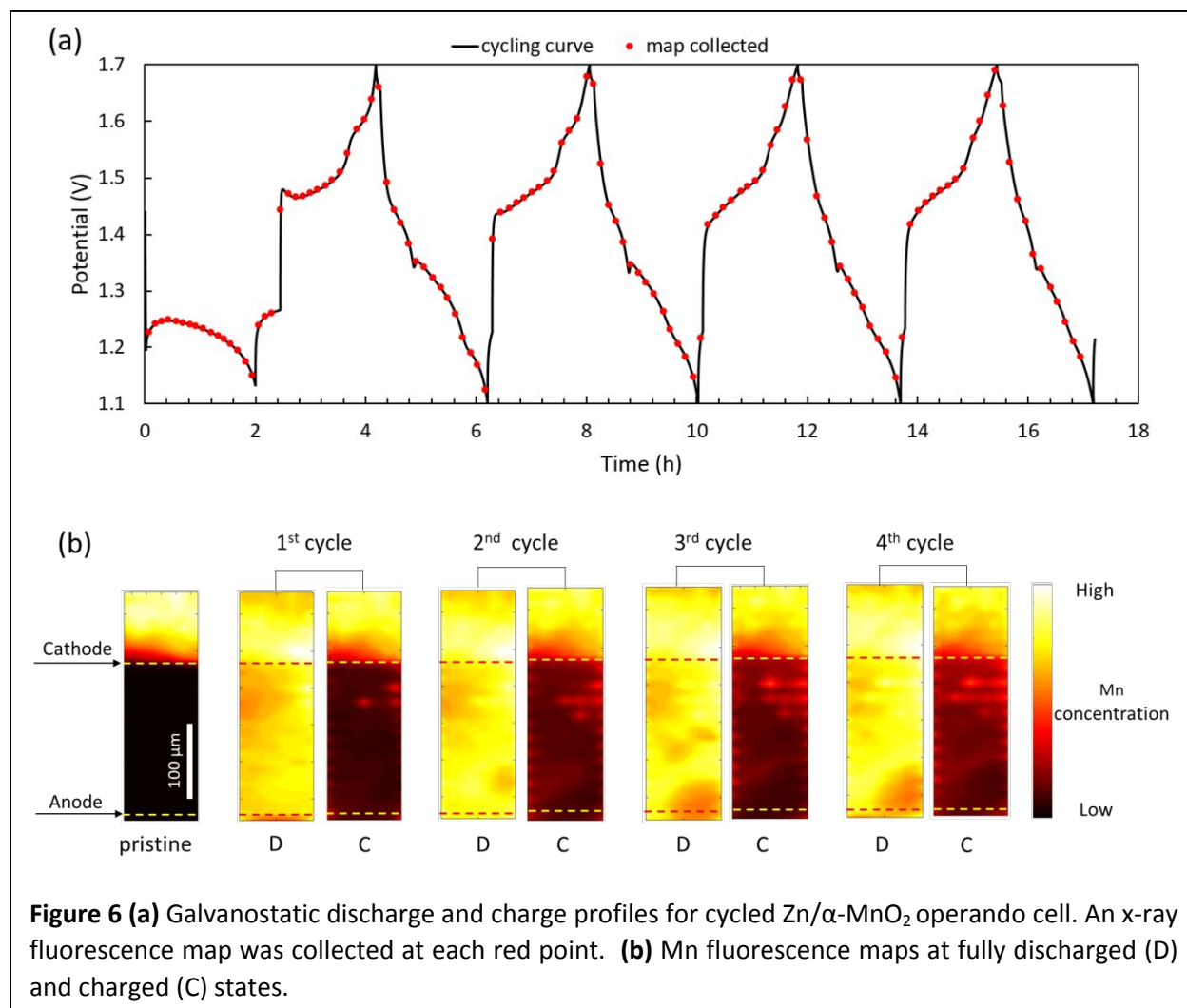


the cathode to the electrolyte is directly associated with the electrochemical process when current is applied. Notably, the corresponding ZHS deposition/dissolution upon discharge/charge has been previously shown by *in-situ* pH monitoring of ZnSO₄ electrolyte in a Zn/ α -MnO₂ cell to originate from induced local pH changes in the electrolyte during Galvanostatic cycling.⁶⁰ Sustained capacity retention of the Zn/MnO₂ system will require successful dissolution/deposition of both ZHS and manganese species.

Evidence and quantification of dissolution-deposition reaction mechanism

A second *operando* experiment was performed to quantify Mn dissolution during multiple galvanostatic cycles. A Zn/ α -MnO₂ *operando* cell was discharged and charged for 5 cycles (ending on the 5th discharge) with Mn fluorescence maps collected every ~9 minutes (**Figure 6, Figure S9, Supplemental Video**). **Figure 6(a)** indicates the positions on the voltage curves where the maps were collected where over 100 maps were recorded during the 5 cycles. In each cycle, a significant increase in the intensity of Mn in the electrolyte is observed during discharge with corresponding decrease during charge. The Mn

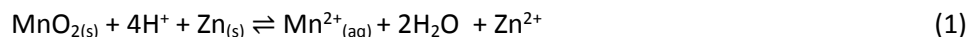
intensity maps of the *operando* cell at fully discharged (D) and charged (C) states are shown in **Figure 6(b)**. In the fully discharged state of each cycle, the Mn intensity is high. In contrast, the Mn intensity is low in the fully charged state. Thus, **Figure 6(b)** provides a direct visualization of a reversible Mn dissolution-deposition reaction in the Zn/ α -MnO₂ system.



Mn fluorescence intensity can be related to Mn concentration in the electrolyte.⁶¹ To quantify relationship between Mn fluorescence intensity and concentration for the *operando* experiment in **Figure 6**, a Mn calibration curve was measured. Calibration standards were prepared inside the *operando* cell configuration consisting of the Zn foil, glass fiber separator, 2 M ZnSO_{4(aq)}, and MnSO_{4(aq)} with known concentrations. The relationship between Mn fluorescence intensity and MnSO₄ concentration is shown in **Figure 7(a)**. Two linear regimes are noted from 0.01 M to 0.5 M and 0.7 M to 1.5 M, providing two equations with distinct slopes. Similar two-regime linear correlations between metal ion concentration in aqueous solution and x-ray fluorescence intensity has been observed previously.⁶²

Based on the calibration curve (**Figure 7(a)**), the average Mn concentration in the *operando* cell electrolyte for each map was calculated using the average Mn fluorescence intensity mapped per

electrolyte area (**Figure 7(b)**). Additionally, the Mn concentration was estimated assuming Mn dissolution and deposition to be the sole redox reaction in the system (**Equation (1)**).



The observed and estimated Mn concentrations are compared in **Figure 7(c)**. The Mn concentration increases upon discharge consistent with the proposed dissolution mechanism. Upon charge the Mn concentration decreases, though does not fully return to the original value. Under these electrochemical test conditions, the Mn concentration after charge increases slightly with each cycle. This implies that more Mn is reduced and dissolved than is oxidized and deposited on charge. These results are consistent with the cycle data, which show higher discharge than charge capacities for the first 5 cycles (**Figure 2 (b)**). The x-ray fluorescence mapping results (**Figure 7 (c)**) suggest ~70% of the α - MnO_2 electrode dissolves on discharge. Notably, the observed Mn concentration is higher than estimated at full discharge and slightly lower at full charge. This observation may be the result of a local concentration gradient in the cell electrolyte. In **Figure S11**, the local Mn fluorescence intensities were sampled from locations near

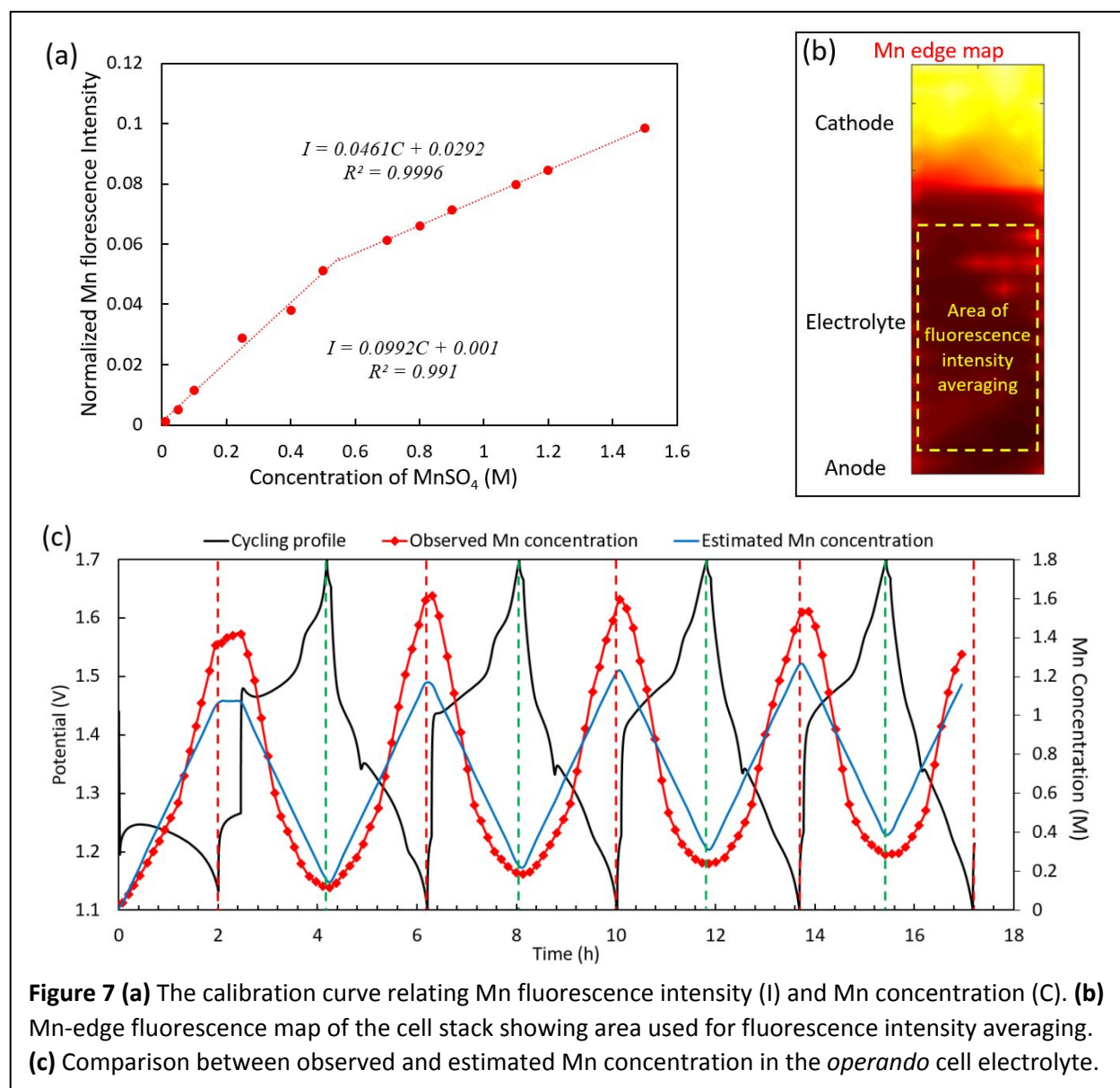
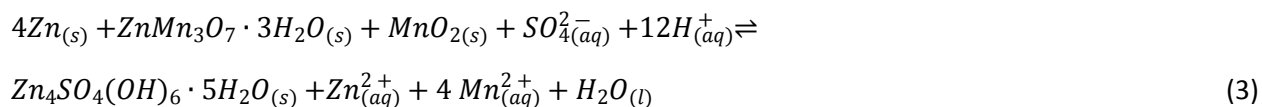
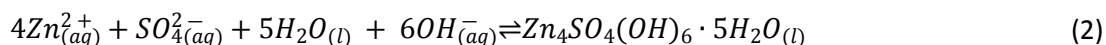
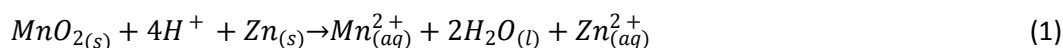


Figure 7 (a) The calibration curve relating Mn fluorescence intensity (I) and Mn concentration (C). **(b)** Mn-edge fluorescence map of the cell stack showing area used for fluorescence intensity averaging. **(c)** Comparison between observed and estimated Mn concentration in the *operando* cell electrolyte.

the cathode and near the anode then converted to Mn concentration using the calibration curve. The Mn concentration near the anode is lower than the Mn concentration at the cathode, consistent with Mn dissolution originating at the cathode. The difference in the Mn concentration gradient is especially apparent after cycle 2 on discharge and charge. Thus, differences between the observed and estimated Mn concentration in **Figure 7(c)** may relate to the diffusion of Mn ions through the electrolyte from the cathode to anode. Additionally, the Mn K-edge XANES spectra in the electrolyte measured after the first and fourth discharge are highly consistent with the XANES spectra of 0.8 M MnSO₄ standard solution in 2 M ZnSO₄ (**Figure S12**), confirming that the dissolved Mn species is Mn²⁺.

The quantitative *operando* x-ray fluorescence maps demonstrate an increase of manganese in the electrolyte on reduction (discharge) and a decrease in the dissolved manganese on charge. The XRD of the *ex-situ* α-MnO₂ discharged samples did not show the formation of a zinc inserted manganese oxide phase. Rather, XRD and XAS analyses of the charged cathodes after the 5th cycle indicate the presence of a DFT-derived broken tunnel α-MnO₂⁵⁴ and a Zn-inserted layered chalcophanite (ZnMn₃O₇·3H₂O)⁴⁵ phase.

Thus, the following reactions are suggested based on the results of *operando* x-ray fluorescence and *ex-situ* XANES, EXAFS, XRD, TEM and SAED. Upon discharge, reaction (1) takes place with reduction of Mn⁴⁺ and consumption of protons from the electrolyte. The local pH change induced by proton consumption results in chemical reaction (2) leading to ZHS precipitation. Upon charge, ZHS dissolves and Mn²⁺ is oxidized, where solid manganese oxide phases, consisting of a broken tunnel variant of α-MnO₂ and a Zn-inserted layered chalcophanite (ZnMn₃O₇·3H₂O) (reaction 3) are deposited on the cathode surface.



The observed Mn concentration changes in the electrolyte during cycling indicate that the dissolution-deposition reaction is the main contributor to cell capacity, rather than Zn²⁺ or H⁺ conversion or insertion.

Previous reports suggest Mn²⁺ dissolution limits the cycle life of Zn/MnO₂ cells with ZnSO₄ electrolyte and suggest Mn²⁺ electrolyte additives, such as MnSO₄, can suppress Mn dissolution and improve capacity retention.^{5, 18, 26, 27, 63} However, considering the reversible dissolution-deposition process to be the dominant electrochemical reaction, the addition of Mn²⁺ to the electrolyte in Zn/MnO₂ batteries is equivalent to introducing extra active material into the system, consequently providing additional capacity rather than improving the capacity retention through reduced dissolution (**Figure S13**). Extended cycling of the parent Zn/MnO₂ system is provided in **Figure S14**. Elucidation of the mechanism herein provides insight for approaches to enhance capacity retention.

Conclusion

In this study, we investigated synthetic potassium-containing α - MnO_2 , $\text{K}_{0.97}\text{Mn}_8\text{O}_{16}\cdot 0.56\text{H}_2\text{O}$, as a cathode material for an aqueous Zn/ α - MnO_2 battery with mildly acidic 2 M ZnSO_4 aqueous electrolyte. *Operando* x-ray fluorescence mapping was conducted to obtain time resolved and quantitative measurement of the Mn concentration in the electrolyte as a function of discharge and charge. Upon discharge, the Mn^{4+} dissolved from the cathode and was detected in the electrolyte as Mn^{2+} . Upon charge, solid manganese oxide deposited on the cathode and were identified as a broken tunnel variant of α - MnO_2 and a Zn-inserted layered chalcophanite phase ($\text{ZnMn}_3\text{O}_7\cdot 3\text{H}_2\text{O}$). These results demonstrate experimentally for the first time, that a reversible dissolution-deposition mechanism is the quantitatively dominant electrode reaction for an aqueous potassium-containing Zn/ α - MnO_2 battery. Understanding the dominant electrochemical process of the Zn/ MnO_2 battery can enable future solutions toward improving cycle life and its potential as a high energy density, low cost, and environmentally-friendly chemistry for stationary energy storage.

Supplemental Information

Data included in the supplemental information section are x-ray diffraction (XRD), thermogravimetric analysis (TGA) data for as synthesized α - MnO_2 , Rietveld refinement results for as-prepared and cycled electrodes, coordination numbers and interatomic distances determined from EXAFS fits, and electrochemistry comparisons between coin-type and operando cells. Also provided is a video of the *operando* XAS results displayed in Figure 6.

Acknowledgement

This work was supported as part of the Center for Mesoscale Transport Properties, an Energy Frontier Research Center supported by the U.S. Department of Energy, Office of Science, Basic Energy Sciences via grant #DE-SC0012673. The extended cycling and electrolyte additive electrochemistry studies were supported by the Department of Energy, Office of Electricity, administered through Sandia National Laboratories, Purchase Order #1955692. The authors thank A. Brady, K. Tallman and P. Liu for providing the broken tunnel cryptomelane structure used for Rietveld refinement. The microscopes used for the study were supported by the U.S. Department of Energy (DOE), Office of Basic Energy Sciences, under Contract No. DE-SC0012704. The synchrotron measurements were conducted at the X-ray Fluorescence Microprobe (XFM, 4-BM) and the Quick X-ray Absorption and Scattering (QAS, 7-BM) of the National Synchrotron Light Source II (NSLS-II) which is a U.S. DOE Office of Science Facility, at Brookhaven National Laboratory under Contract No. DE-SC0012704. EST acknowledges support from the William and Jane Knapp Chair in Energy and the Environment.

References

1. P. F. Smith, K. J. Takeuchi, A. C. Marschilok and E. S. Takeuchi, *Accounts of Chemical Research*, 2017, **50**, 544-548.
2. T. M. Gur, *Energy Environ. Sci.*, 2018, **11**, 2696-2767.
3. M. Armand and J. M. Tarascon, *Nature*, 2008, **451**, 652-657.
4. R. M. Wittman, M. L. Perry, T. N. Lambert, B. R. Chalamala and Y. Preger, *Journal of The Electrochemical Society*, 2020, **167**, 090545.
5. H. Pan, Y. Shao, P. Yan, Y. Cheng, K. S. Han, Z. Nie, C. Wang, J. Yang, X. Li, P. Bhattacharya, K. T. Mueller and J. Liu, *Nature Energy*, 2016, **1**, 16039.
6. C. Xu, B. Li, H. Du and F. Kang, *Angewandte Chemie International Edition*, 2012, **51**, 933-935.

7. J. S. Ko, M. B. Sassin, J. F. Parker, D. R. Rolison and Jeffrey W. Long, *Sustainable Energy & Fuels*, 2018, **2**, 626-636.
8. G. Fang, C. Zhu, M. Chen, J. Zhou, B. Tang, X. Cao, X. Zheng, A. Pan and S. Liang, *Advanced Functional Materials*, 2019, **29**, 1808375.
9. J. W. Gallaway, B. J. Hertzberg, Z. Zhong, M. Croft, D. E. Turney, G. G. Yadav, D. A. Steingart, C. K. Erdonmez and S. Banerjee, *Journal of Power Sources*, 2016, **321**, 135-142.
10. C. Xie, T. Li, C. Deng, Y. Song, H. Zhang and X. Li, *Energy Environ. Sci.*, 2020, **13**, 135-143.
11. S. Zhao, B. Han, D. Zhang, Q. Huang, L. Xiao, L. Chen, D. G. Ivey, Y. Deng and W. Wei, *Journal of Materials Chemistry A*, 2018, **6**, 5733-5739.
12. J. Shin, J. Lee, Y. Park and J. W. Choi, *Chemical Science*, 2020, **11**, 2028-2044.
13. M. Chen, G. Feng and R. Qiao, *Current Opinion in Colloid & Interface Science*, 2020, **47**, 99-110.
14. D. Bin, Y. Wen, Y. Wang and Y. Xia, *Journal of Energy Chemistry*, 2018, **27**, 1521-1535.
15. X.-P. Gao and H.-X. Yang, *Energy Environ. Sci.*, 2010, **3**, 174-189.
16. L. Wang and J. Zheng, *Materials Today Advances*, 2020, **7**, 100078.
17. G. Liang, F. Mo, H. Li, Z. Tang, Z. Liu, D. Wang, Q. Yang, L. Ma and C. Zhi, *Advanced Energy Materials*, 2019, **9**, 1901838.
18. S. H. Kim and S. M. Oh, *Journal of Power Sources*, 1998, **72**, 150-158.
19. G. Li, Z. Huang, J. Chen, F. Yao, J. Liu, O. L. Li, S. Sun and Z. Shi, *J. Mater. Chem. A*, 2020, **8**, 1975-1985.
20. C. Qiu, X. Zhu, L. Xue, M. Ni, Y. Zhao, B. Liu and H. Xia, *Electrochimica Acta*, 2020, **351**, 136445.
21. C. F. Bischoff, O. S. Fitz, J. Burns, M. Bauer, H. Gentischer, K. P. Birke, H.-M. Henning and D. Biro, *Journal of The Electrochemical Society*, 2020, **167**, 020545.
22. S. Ching, J. L. Roark, N. Duan and S. L. Suib, *Chemistry of Materials*, 1997, **9**, 750-754.
23. S. Ching and S. L. Suib, *Comments on Inorganic Chemistry*, 1997, **19**, 263-282.
24. B. Lee, C. S. Yoon, H. R. Lee, K. Y. Chung, B. W. Cho and S. H. Oh, *Scientific Reports*, 2014, **4**, 6066.
25. B. Lee, H. R. Lee, H. Kim, K. Y. Chung, B. W. Cho and S. H. Oh, *Chemical Communications*, 2015, **51**, 9265-9268.
26. W. Sun, F. Wang, S. Hou, C. Yang, X. Fan, Z. Ma, T. Gao, F. Han, R. Hu, M. Zhu and C. Wang, *Journal of the American Chemical Society*, 2017, **139**, 9775-9778.
27. N. Zhang, F. Cheng, J. Liu, L. Wang, X. Long, X. Liu, F. Li and J. Chen, *Nature Communications*, 2017, **8**, 405.
28. L. M. Housel, L. Wang, A. Abraham, J. Huang, G. D. Renderos, C. D. Quilty, A. B. Brady, A. C. Marschilok, K. J. Takeuchi and E. S. Takeuchi, *Accounts of Chemical Research*, 2018, **51**, 575-582.
29. Y. Huang, J. Mou, W. Liu, X. Wang, L. Dong, F. Kang and C. Xu, *Nano-Micro Letters*, 2019, **11**, 49.
30. X. Gao, H. Wu, W. Li, Y. Tian, Y. Zhang, H. Wu, L. Yang, G. Zou, H. Hou and X. Ji, *Small*, 2020, **n/a**, 1905842.
31. C. Xu, H. Du, B. Li, F. Kang and Y. Zeng, *Electrochemical and Solid-State Letters*, 2009, **12**, A61-A65.
32. B. Lee, H. R. Lee, H. Kim, K. Y. Chung, B. W. Cho and S. H. Oh, *Chem. Commun. (Cambridge, U. K.)*, 2015, **51**, 9265-9268.
33. W. Sun, F. Wang, S. Hou, C. Yang, X. Fan, Z. Ma, T. Gao, F. Han, R. Hu, M. Zhu and C. Wang, *J. Am. Chem. Soc.*, 2017, **139**, 9775-9778.
34. A. S. Poyraz, J. Laughlin and Z. Zec, *Electrochimica Acta*, 2019, **305**, 423-432.
35. X. Guo, J. Zhou, C. Bai, X. Li, G. Fang and S. Liang, *Materials Today Energy*, 2020, **16**, 100396.
36. X. Li, M. Banis, A. Lushington, X. Yang, Q. Sun, Y. Zhao, C. Liu, Q. Li, B. Wang, W. Xiao, C. Wang, M. Li, J. Liang, R. Li, Y. Hu, L. Goncharova, H. Zhang, T.-K. Sham and X. Sun, *Nature Communications*, 2018, **9**, 4509.

37. S.-M. Bak, Z. Shadiké, R. Lin, X. Yu and X.-Q. Yang, *NPG Asia Materials*, 2018, **10**, 563-580.
38. F. Lin, Y. Liu, X. Yu, L. Cheng, A. Singer, O. G. Shpyrko, H. L. Xin, N. Tamura, C. Tian, T.-C. Weng, X.-Q. Yang, Y. S. Meng, D. Nordlund, W. Yang and M. M. Doeff, *Chemical Reviews*, 2017, **117**, 13123-13186.
39. K. R. Adair, M. N. Banis, Y. Zhao, T. Bond, R. Li and X. Sun, *Advanced Materials*, 2020, **32**, 2002550.
40. R. Robert, D. Zeng, A. Lanzirrotti, P. Adamson, S. J. Clarke and C. P. Grey, *Chemistry of Materials*, 2012, **24**, 2684-2691.
41. J. Luo, H. T. Zhu, H. M. Fan, J. K. Liang, H. L. Shi, G. H. Rao, J. B. Li, Z. M. Du and Z. X. Shen, *The Journal of Physical Chemistry C*, 2008, **112**, 12594-12598.
42. B. Toby and R. Dreele, *Journal of Applied Crystallography*, 2013, **46**, 544-549.
43. B. Ravel and M. J. Newville, *J. Synchrotron Radiat.*, 2005, **12**, 537-541.
44. J. Vicat, E. Fanchon, P. Strobel and D. Tran Qui, 1986, **42**, 162-167.
45. A. D. Wadsley, *Nature*, 1953, **172**, 1103-1104.
46. J. J. Rehr, J. Mustre de Leon, S. I. Zabinsky and R. C. Albers, *J. Am. Chem. Soc.*, 1991, **113**, 5135.
47. M. Newville, *Journal of Physics: Conference Series*, 2013, **430**, 012007.
48. K. Momma and F. Izumi, *Journal of Applied Crystallography*, 2011, **44**, 1272-1276.
49. J. Chen, X. Tang, J. Liu, E. Zhan, J. Li, X. Huang and W. Shen, *Chemistry of Materials*, 2007, **19**, 4292-4299.
50. H. Huang, Y. Meng, A. Labonte, A. Doble and S. L. Suib, *The Journal of Physical Chemistry C*, 2013, **117**, 25352-25359.
51. K. Momma and F. Izumi, *Journal of Applied Crystallography*, 2011, **44**, 1272-1276.
52. J. Vicat, E. Fanchon, P. Strobel and D. Tran Qui, *Acta Crystallographica Section B*, 1986, **42**, 162-167.
53. Z. Fathi, R. Khavari-Nejad, H. Mahmoodzadeh and T. Satari, *Journal of Plant Protection Research*, 2017, **57**.
54. A. B. Brady, K. R. Tallman, E. S. Takeuchi, A. C. Marschilok, K. J. Takeuchi and P. Liu, *The Journal of Physical Chemistry C*, 2019, **123**, 25042-25051.
55. J. Post, *American Mineralogist*, 1988, **73**, 1401-1404.
56. A. S. Poyraz, J. Huang, C. J. Pelliccione, X. Tong, S. Cheng, L. Wu, Y. Zhu, A. C. Marschilok, K. J. Takeuchi and E. S. Takeuchi, *Journal of Materials Chemistry A*, 2017, **5**, 16914-16928.
57. Y. Yuan, A. Nie, G. M. Odegard, R. Xu, D. Zhou, S. Santhanagopalan, K. He, H. Asayesh-Ardakani, D. D. Meng, R. F. Klie, C. Johnson, J. Lu and R. Shahbazian-Yassar, *Nano Letters*, 2015, **15**, 2998-3007.
58. A. S. Poyraz, J. Huang, S. Cheng, D. C. Bock, L. Wu, Y. Zhu, A. C. Marschilok, K. J. Takeuchi and E. S. Takeuchi, *Green Chemistry*, 2016, **18**, 3414-3421.
59. R. Zhang, X. Yu, K.-W. Nam, C. Ling, T. S. Arthur, W. Song, A. M. Knapp, S. N. Ehrlich, X.-Q. Yang and M. Matsui, *Electrochemistry Communications*, 2012, **23**, 110-113.
60. B. Lee, H. R. Seo, H. R. Lee, C. S. Yoon, J. H. Kim, K. Y. Chung, B. W. Cho and S. H. Oh, *ChemSusChem*, 2016, **9**, 2948-2956.
61. J. Lakowicz, *Principles of Fluorescence Spectroscopy*, 2006, Springer US.
62. S. Dubrovka, S. Chursin and V. Verkhoturova, *Journal of Physics: Conference Series*, 2017, **781**, 012015.
63. M. Han, J. Huang, S. Liang, L. Shan, X. Xie, Z. Yi, Y. Wang, S. Guo and J. Zhou, *iScience*, 2020, **23**, 100797.